13 Surface Physics

T. Greber, M. Hengsberger, J. Wider, H. J. Neff, F. Baumberger, M. Hoesch, W. Auwärter, M. Muntwiler, A. Tamai, A. Dolocan, M. Barry, T. Gresch, W. Deichmann, J. Osterwalder

Artificial nanostructures, exemplified e.g. by ultrathin films, quantum wires or quantum dots, are of enormous scientific and technological interest. Their electronic and magnetic properties are dominated by size- and shape dependent quantum effects and can thus be tailored to fulfil any particular need. Their diameter in at least one dimension does not exceed a few atomic layers, and therefore they consist to a large extent of interfaces and surfaces.

In the surface physics laboratory we prepare clean surfaces, ultrathin films and nanostructures under ultrahigh vacuum (UHV) conditions and characterize their surface and interface structures at atomic resolution. Their electronic and magnetic properties are studied in detail. In order to measure the geometric arrangement of the atoms within the first few monolayers of the surface we apply predominantly electron-based techniques such as x-ray photoelectron diffraction (XPD), medium-energy electron diffraction (MEED), low-energy electron diffraction (LEED), and more recently also scanning-tunneling microscopy (STM). Angle-resolved photoemission spectroscopy (ARPES) gives us a detailed picture of the electronic band structure of such systems. Specifically, our experimental setup permits to directly map sections through the Fermi surface, which describes the electronic degrees of freedom relevant for transport properties, magnetic interactions and phase transitions. An important asset of such experiments is that the same probe (photoemission) gives us structural, electronic and magnetic information, and we can therefore study the interplay between these different degrees of freedom on the same sample.

The research carried out during the last year can be grouped into four topics:

- *Clean metal surfaces and surface states*
  The close-packed (111) surfaces of several face-centred-cubic metals (e.g. Au, Ag, Cu, Ni) exhibit so-called Shockley surface states that propagate almost freely within the surface plane, and which have wave functions that decay exponentially both into the vacuum and into the bulk of the crystal. They thus exemplify a two-dimensional gas of nearly-free electrons (2DEG), which manifests itself in parabolic energy dispersion relations. We have continued to study the responses of these 2DEG to various internal or external perturbations. The Shockley state on Ni(111) is particularly difficult to study because it is just marginally occupied and extremely susceptible to surface contamination. On the other hand, it is a most interesting case because it sits on a ferromagnetic substrate. In Section 13.1 high resolution spectra are presented and the temperature dependence of the binding energy is discussed.
  On Au(111), a splitting of this same Shockley state has been explained in terms of the spin-orbit interaction. With our new COmplete PHotoEmission Experiment (COPHEE), which is now set up at the Swiss Light Source (SLS) in Villigen, we were able to reproduce this splitting (Section 13.2) and to establish for the first time the detailed spin structure in which the electron spin is coupled to the two-dimensional electron momentum.
  Vicinal Cu(111) surfaces expose (111)-oriented terraces separated by a roughly regular array of monoatomic steps; therefore they represent lateral nanostructures that can be easily prepared. For the Shockley state this regular step lattice represents a periodic repulsive potential. On Cu(443) the coherent motion of the electrons in this lattice leads to the formation of an energy gap at the Fermi energy (Section 13.3).
  Photoemission spectra from clean crystal surfaces contain not only signals from such surface states, but also strong emission from bulk states that exhibit dispersion in all three dimensions.

For this highly surface-sensitive technique, the question arises whether these bulk states correspond to the Bloch states of the sample volume that extend to infinity in all three dimensions. Our experiments at the SPring-8 synchrotron in Japan, where we measured such bulk states on Ni(111) at higher photon energies, indicate that the normal low-energy ARPES experiments probe bulk-like states that feel the presence of the surface (Section 13.4).

- *Ultrathin films*
  The preparation of well-defined monolayer-thick films permits us to study the structural, electronic and magnetic properties at an interface between two different materials. In the nanosciences, such knowledge is essential for the understanding of how nanoscale structures and devices function. In the case of a single lead layer on Cu(111), the film takes the role of a so-called surfactant, i.e. it promotes the layer-by-layer growth of other transition metals while the lead keeps floating on top of the growing film. In Section 13.5 it is tried to rationalize the surfactant effect with features in the detailed electronic structure of the film.
  Nickel monolayers on Cu(001) represent building blocks for new magnetic devices based on the spin-filter effect and oscillatory exchange coupling. In Section 13.6 it is shown how the Fermi surface of nickel evolves as a function of film thickness, and also how the magnetic state of the film transforms from paramagnetic to ferromagnetic.
  Lastly, we have continued to study single monolayers of hexagonal boron nitride on Ni(111) that provide a well-defined model case for an insulating monolayer on top of a ferromagnetic substrate. In Section 13.7 it is shown that linear defects in the film can be correlated to the occurrence of two different structural domains, and how the detailed structure at the domain boundaries can be inferred from combined STM and XPD measurements.

- *Adsorbed molecules*
  Molecular monolayers offer a highly interesting route to prepare functionalized surfaces. Chemists provide molecules with suitable chemical anchors and with the desired functional groups that are to be exposed at the surface. We are working on methods that can measure the bonding geometry of the molecules on the substrate, and we study the electronic properties of molecular layers that have a high degree of self-organized crystalline order within the layer. As a first example, Section 13.8 presents STM and XPD data from C_{60} monolayers on a stepped Cu(221) surface. The steps have a two-fold function: they align the molecules in one-dimensional chains, and they lock the individual molecules into a single, well-defined orientation.
  In Section 13.9 the adsorption geometry of cysteine, a small amino acid, is investigated by a new generation XPD experiment that makes use of the high-brightness tuneable synchrotron radiation of the SLS. The XPD patterns display directly the chiral character of the molecule when single enantiomers are adsorbed.

- *Time-resolved electron diffraction*
  The experimental setup for our picosecond time-resolved electron diffraction experiment has been completed with the installation of the laser pulse amplifier. First tests have been carried out for pump-probe experiments in which a sample is excited by a laser pump pulse and probed, after a defined delay, by a low-energy electron pulse to monitor ultrafast structural changes at the sample surface. These tests have brought forward various new experimental difficulties that need to be overcome. In Section 13.10 some of these problems and their solutions are described.
  Finally, Section 13.11 reports the development and testing of a laser pulse autocorrelator, which is an important diagnostic device for characterizing the temporal width and the coherence time of the pulses.

13.1 Temperature dependence of the Shockley surface state on Ni(111)

in collaboration with:
G. Grad and P. Blaha, Institut für Physikalische und Theoretische Chemie, TU Wien

The Shockley surface state on Ni(111) is partially occupied and exchange split [1]. This is particularly interesting with respect to the question on how these electrons that do not propagate in the bulk and that have predominant sp-character do couple to the underlying exchange split band structure. Density functional calculations predict a very small exchange splitting of 23 meV and an energy upshift of 143 meV for majority and 120 meV for minority electrons in going from the ferromagnetic to the paramagnetic state [2]. Figure 13.1 shows angular resolved photoemission data of the Shockley surface state and its temperature dependence. Our instrument exposes photoemission from band states up to $5k_BT$ above the Fermi level. The binding energy of the surface state at the $\bar{\Gamma}$-point of the surface reciprocal lattice, i.e. at normal emission, is 45$\pm$5 meV at room temperature. We do not see an exchange splitting in these spin-integrated experiments. At room temperature the exchange splitting would therefore have to be greater than 130 meV or less than 60 meV. The upper bound is given by the limitation of our photoemission experiment to $5k_BT$ above the Fermi level and the lower value is estimated from the peak width that might contain unresolved spin up and spin down components. For the temperature dependence, we find a strong increase of the energy of the surface state at $\bar{\Gamma}$ up to the Curie temperature of Ni (631 K). This increase is in fair agreement with the theoretical prediction. The drop of the increase rate coincides within the accuracy of the experiment with the Curie temperature that was inferred from the temperature dependence of a simultaneously measured bulk band. The center of gravity of the surface state peak at $\bar{\Gamma}$ crosses the Fermi level at $365 \pm 30K$. In the paramagnetic phase the temperature coefficient for the binding energy change is reduced by a factor of 9 and is close to corresponding values on noble metal surfaces [3].

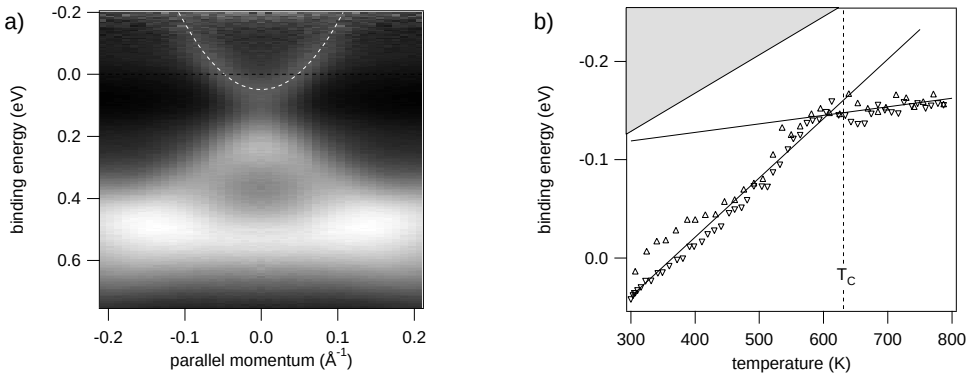

Figure 13.1: *$He\ I\alpha$ excited angular resolved photoemission data from Ni(111).*
a) Polar scan around normal emission at room temperature. The Fermi level (horizontal line) and the Shockley surface state (parabola) are emphasized with dashed lines.
b) Temperature dependence of the surface state binding energy at $\bar{\Gamma}$, i.e. at the bottom of the parabola. Triangles indicate data recorded during temperature rise ($\triangle$) and fall ($\triangledown$), respectively. The dark area $(E_F - E) > 5k_BT$ is not accessible in our photoemission experiment.

[1] M. Donath, F. Passek, V. Dose, Phys. Rev. Lett. **70** (1993) 2802.
[2] G. Grad and P. Blaha, work in progress.
[3] R. Paniago, R. Matzdorf, G. Meister and A. Goldmann, Surf. Sci. **336** (1995) 113.

13.2 Spin and angular resolved photoemission of the surface state on Au(111)

in collaboration with: V.N. Petrov, St. Petersburg Technical University, Russia and L. Patthey, M. Shi and M. Falub, Swiss Light Source, Paul Scherrer Institut, 5232 Villigen, Switzerland

The (111) surface of gold accommodates a Shockley-type surface state as well. In this case, the two-dimensional quasi-free electron gas is subject to a strong spin-orbit splitting proportional to the in-plane momentum of the electrons [1; 2]. In momentum space this results in a shift of the parabolic dispersions for spin-up and spin-down electrons.

In the beginning of 2003 the spin-resolved photoemission spectrometer COPHEE ("the COmplete PHotoEmission Experiment") was installed at the Surface and Interface Spectroscopy (SIS) beamline at the Swiss synchrotron Light Source (SLS). A first beam-time was devoted to spin-resolved measurements of the surface state on Au(111). In addition, the spin-integrating channeltron detector of COPHEE was used to investigate the performance of the spectrometer in conjunction with synchrotron radiation. Figure 13.2 shows the measured dispersion and Fermi surface of the surface state on Au(111). The splitting is nicely resolved in both data sets. The identification of the spin character

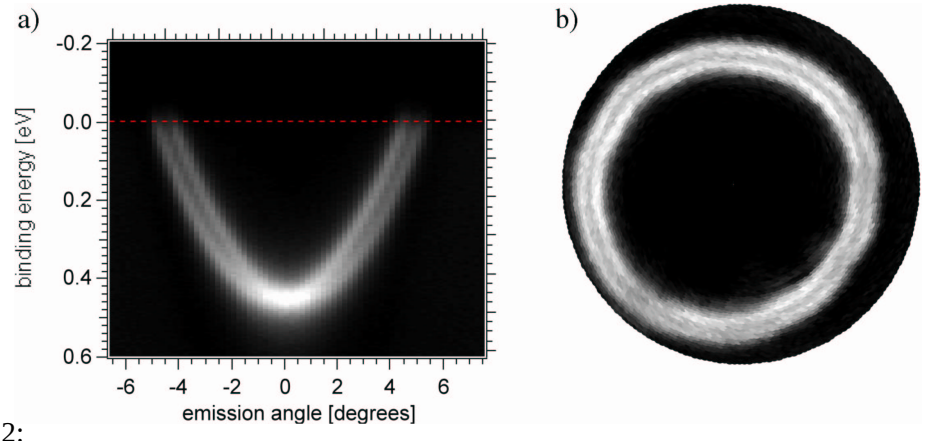

Figure 13.2:
a) Photoemission dispersion map of the surface state on Au(111). The dataset consists of photoemission spectra taken at various emission angles at a photon energy of $h\nu$=21.1 eV.
b) Fermi-surface map of this same surface state. The angular distribution of photoelectrons emitted from slightly below the Fermi edge into a small cone around normal emission (7° opening angle) is shown in a linear grey-scale in parallel projection. The sample was cooled using liquid nitrogen during the acquisition of both data sets.

of the two subbands is a direct probe of the spin-orbit interaction theory that has been inferred to describe the measured band splitting [1; 2]. Figure 13.3 shows spin-resolved photoemission spectra of the surface state on Au(111) at normal emission and positive and negative emission angles. At normal emission, no splitting is observed and the spin-up and spin-down spectra coincide. For off-normal emission, the splitting reveals itself by the presence of distinct spin-up and spin-down peaks that are shifted with respect to each other. A spin-resolved Fermi surface map (not shown) furthermore confirms the detailed spin structure that had been proposed, with in-plane spin vectors rotating tangentially along the Fermi surface contours, and with no out-of-plane component.

[1] S. LaShell, B.A. MacDougall, E. Jensen, Phys. Rev. Lett. **77** (1996) 3419.
[2] G. Nicolay, F. Reinert, S. Hüfner, P. Blaha, Phys. Rev. B **65** (2001) 33407.

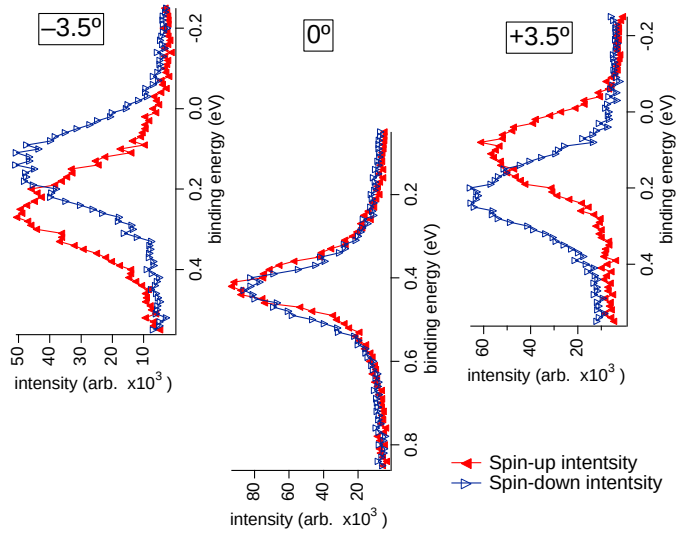

Figure 13.3: *Spin-resolved photoemission spectra of the surface state on Au(111) at different polar emission angles. The spectrometer resolution was relaxed for the acquisition of these data sets to allow for the reduced sensitivity associated with spin analysis and corresponding longer integration times. Each data set was recorded in less than two hours.*

13.3 Observation of a step induced gap in the Fermi surface of vicinal Cu(443)

in collaboration with:
J. Krempasky, M. Shi and L. Patthey, Swiss Light Source, Paul Scherrer Institut, Villigen

On vicinal Cu(111) surfaces, the Shockley surface state interacts with the steps that separate the subsequent (111) terraces. The step lattice acts like a periodic repulsive potential that confines the surface state [1; 2; 3]. Correspondingly its maximum binding energy decreases with increasing step density. The surface state is metallic and there is a critical step-step separation ℓ which is equal to the half of the Fermi wave length. At this shape resonance the formation of a gap is expected. This should cause an anisotropy of the electron transport at the surface and, more importantly, give a direct measure for the energy gain of the system due to the ordered step lattice. At room temperature this critical length is best met for Cu(443) ($\ell = 16.3$Å). In the framework of the pilot project *Surface-bulk coupling on vicinal Cu(111)* at the Swiss light source (SLS) we were able to observe for the first time a gap on the Fermi surface of the Shockley surface state resonance.

Fig. 13.4 shows the dispersion plots along the polar emission angle measured for two fixed azimuthal angles: one in the direction perpendicular to the steps (Fig. 13.4(a)) and the other in a plane rotated away by an angle of 18° (Fig. 13.4(b)). The confinement occurs between the steps, and the gap at the Fermi level is seen at $\overline{\Gamma}_{00}$ and $\overline{\Gamma}_{10}$ in Fig.13.4(a). This becomes particularly clear in comparing the data to those in Fig.13.4(b) where, for an azimuthal direction off the step normal, the Shockley surface state band crosses the Fermi level in the second surface Brillouin zone.

[1] O.Sánchez, J.M. García, P. Segovia, J. Alvarez, A.L. Vázquez de Parga, J.E. Ortega, M. Prietsch and R. Miranda, Phys.Rev.B **52**, 7894 (1995).

[2] J.E. Ortega, S. Speller, A.R. Bachmann, A. Mascaraque, E.G. Michel, A. Närmann, A. Mugarza, A. Rubio and F.J. Himpsel Phys.Rev.Lett.**84**, 6110 (2000).

[3] F. Baumberger, T. Greber and J. Osterwalder, Phys.Rev.B **64** (2001) 195411.

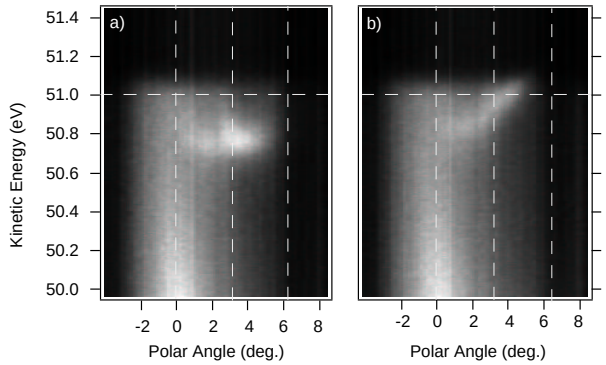

Figure 13.4: *Angular resolved photoemission ($h\nu$=55.5 eV) dispersion plots from the Shockley surface state of Cu(443) (raw data). a) Cut perpendicular to the steps. Clearly, a gap at $\overline{\Gamma}_{00}$ and $\overline{\Gamma}_{10}$ may be observed. The vertical dashed lines indicate projections of planes parallel to the steps which contain $\overline{\Gamma}_{00}$, $\overline{\Gamma}_{10}$ and $\overline{\Gamma}_{20}$, repectively. b) Cut 18° off the direction perpendicular to the steps. A band crossing the Fermi level (horizontal dashed line) in the second surface Brillouin zone is visible. The photoemission data were recorded with the Scienta SES-2002 analyzer in scanning the energy in the angle-dispersive mode. All data were measured at room temperature.*

13.4 Bulk-sensitive band mapping on Ni(111) using high-energy ARPES

in collaboration with:
A. Yamasaki, A. Sekiyama, S. Suga, Osaka University, Japan, and T. Muro, SPring-8, Hyogo, Japan

Photoemission spectroscopy is intrinsically surface sensitive due to the strong interaction of the excited photoelectrons with matter, leading to inelastic mean free paths λ_i of the order of a few atomic layers. This is particularly true for the low photon energies in the range of 20 to 100 eV typically used in ARPES experiments. It has thus been questioned as to how far photoemission can really probe true bulk states [1]. This question has been addressed by comparing ARPES data from Ni(111) measured at low photon energy ($h\nu$ = 21.22 eV), where λ_i is of the order of 6 Å, to higher energy data where λ_i lies between 10 and 20 Å. Such high-energy ARPES experiments at energy and momentum resolutions adequate for band mapping can be performed at beamline BL25U of the SPring-8 synchrotron in Japan.

The experimental ARPES data for three energies, i.e. $h\nu$=21.22 eV, 270 eV, and 497 eV are presented in Fig. 13.5. In the low-energy data (Fig. 13.5a) both the minority (lower binding energy) and majority (higher binding energy) version of the *d* band centered at 1.2 Å^{-1} are exposed [2], though with a far smaller exchange splitting between the two as compared to the density functional theoretical (DFT) curves that are given as red and blue solid lines. In the higher energy data (Figs. 13.5b and c) the same spin-split *d* band pair is observed, with Fermi level crossings at nearly the same $k_{||}$ values for all energies. At these higher energies, the bands can be followed out to higher parallel momenta. The DFT band structure calculations provide an excellent description of the measured band dispersion as far as Fermi level crossings and the general dispersion behaviour are concerned. Regarding the exact band widths and group velocities, however, one notes that the width of the minority *d* band is strongly reduced in the low-energy measurement, while the two high-energy data show a band width that is close to the DFT value. There is also a gradual increase of the exchange splitting between minority and majority *d* bands with photon energy, yet the DFT value of 0.83 eV is not reached at the highest photon energy.

This different behaviour, and the fact that the data obtained with higher-energy photons, and thus

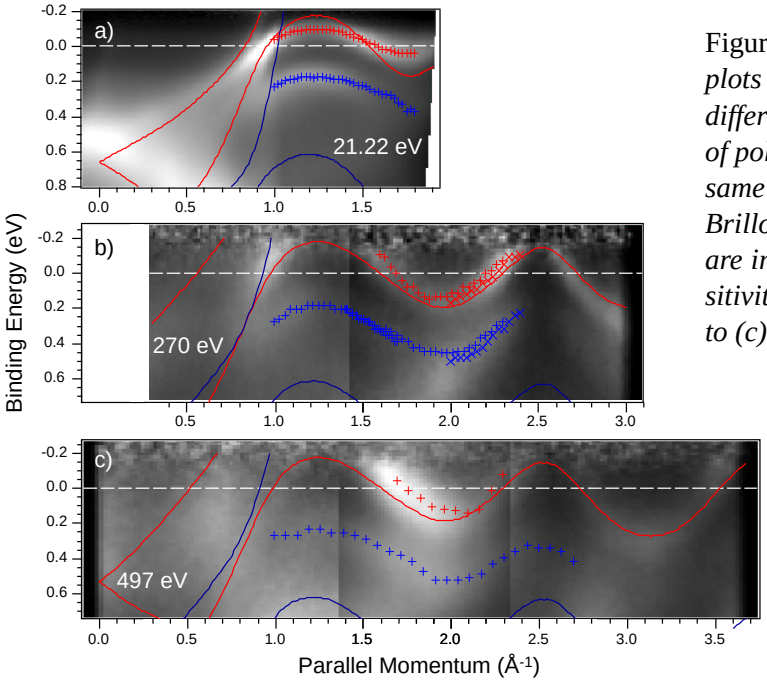

Figure 13.5: *Photoemission dispersion plots from clean Ni(111) measured at different photon energies as a function of polar angle with the goal to probe the same electronic states in different bulk Brillouin zones. The photon energies $h\nu$ are indicated in the figure, the bulk sensitivity increases in going from panel (a) to (c). Red and blue solid lines give minority and majority bands, respectively, as calculated within density functional theory. Red and blue markers indicate measured energy values within some bands as quantified from individual spectra.*

more bulk penetrating photoelectrons, are far better described by the DFT calculations, leads us to the conclusions that ARPES data measured at the typical photon energies of below 100 eV probe bulk bands that are strongly affected by the presence of the surface.

[1] S. Suga, A. Sekiyama, J. Electron Spectrosc. Relat. Phenom. **124**, 81 (2002).

[2] T. Greber, T. J. Kreutz, J. Osterwalder, Phys. Rev. Lett. **79**, 4465 (1997).

13.5 The electronic structure of a surfactant layer: Pb/Cu(111)

Monolayers of Pb promote very efficiently the layer by layer growth of epitaxial films on Cu(111) [1]. For this role as a surfactant the Pb layer must have the properties of a highly elastic skin which is only weakly coupled to the substrate. In order to step beyond the phenomenological understanding of surfactants in terms of lower surface free energy we have investigated the electronic structure of one compact layer of Pb on Cu(111) forming an incommensurate quasi (4×4) structure [2]. Angular resolved photoemission data have been compared with density functional (DFT) calculations [3].

In the Cu(111) Fermi surface map shown in Fig.13.6(a), we readily identify direct transition lines, which are characteristic for the Cu bulk Fermi surface. The contours are well reproduced by a spherical cut through the calculated bulk Fermi surface (Fig.13.6(c)). The most intense circular feature centered at $\bar{\Gamma}$ is due to the free electron like Shockley surface state, which is not reproduced in the bulk calculation. In the data from the lead covered surface (Fig.13.6(b)), the surface state is either quenched or pushed above the Fermi level. Instead, bright features appear in a sixfold symmetric arrangement in the second Brillouin zones of the overlayer 1×1–periodicity. Besides the remaining intensity from the Cu bulk Fermi surface, we observe a weak regular hexagon centered at $\bar{\Gamma}$ with its sides parallel to the surface Brillouin zone and measuring about half its linear dimension. Both features are surprisingly well reproduced in the calculated Fermi surface of a free standing Pb layer (Fig.13.6(d)). This striking similarity shows that adsorbate and substrate electronic systems are

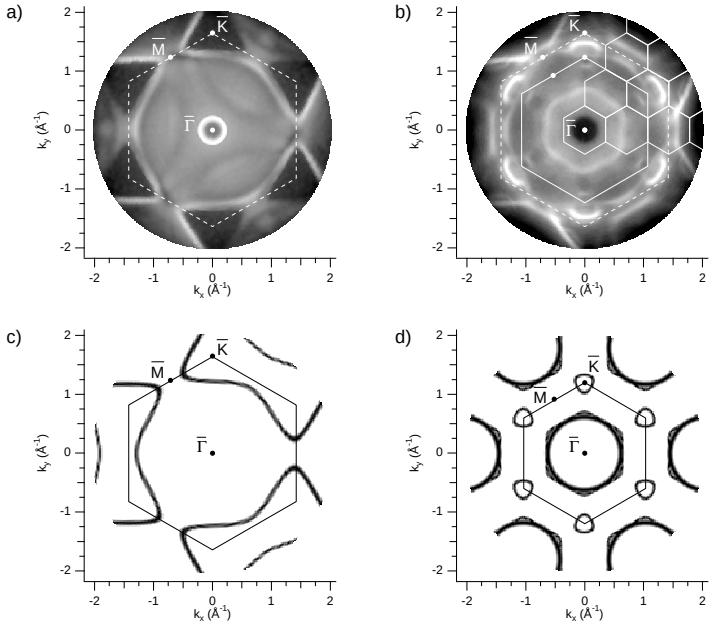

Figure 13.6: *He Iα excited Fermi surface maps of clean Cu(111) (a) and (4×4) Pb/Cu(111) (b). The photoemission intensity is shown on a logarithmic gray scale as a function of the two momentum components in the surface plane. Surface Brillouin zones constructed for the Cu (dashed) and Pb (solid line) periodicities are overlayed. The smaller hexagons in (b) show the nominal Brillouin zones. (c) Cu–bulk Fermi surface, calculated on the spherical k–space contour, defined by the energy of a free-electron-like final state. (d) Fermi surface, as obtained from a density functional calculation for a free-standing planar Pb layer.*

largely decoupled. The reason appears to be the lattice mismatch of ≈33%, which translates into a serious mismatch of the Brillouin zones, relevant inside the Cu(111) surface and inside the Pb layer. The dominant periodicity in the experimental Fermi surface map is clearly the Pb (1×1)–structure. The periodicity of the substrate is not reflected in the adlayer band structure and thus fullfills a requirement for a surfactant, i.e. contributes only weakly to the potential felt by the electrons in the Pb film.

[1] J. Camarero, T. Graf, J.J. de Miguel, R. Miranda, W. Kuch, M. Zharnikov, A. Dittschar, C.M. Schneider, J. Kirschner, Phys. Rev. Lett. **76** (1996) 4428.

[2] S. Müller, J.E. Prieto, C. Rath, L. Hammer, R. Miranda, K. Heinz, J. Phys. Cond. Matter **13** (2001) 1793.

[3] F. Baumberger, A. Tamai, M. Muntwiler, T. Greber, J. Osterwalder, Surf. Sci., in press.

13.6 Fermi-surface mapping on ultrathin films of Ni/Cu(001)

in collaboration with: V.N. Petrov, St. Petersburg Technical University, Russia

Ultrathin films of Ni on Cu(001) have recently attracted a lot of interest, because of their rich magnetic behaviour. At very low film thickness the electronic structure of the films is interesting by itself because the electronic states observed in photoelectron spectroscopy clearly derive from nickel but despite the low film thickness they show behaviour very similar to three-dimensional bulk nickel [1]. One study even reports a bulk-like Fermi surface down to the ultimate limit of a monolayer [2]. Tri-layers of Ni/Cu/Ni also show a giant magneto-resistance effect, which depends on the thickness of the Cu spacer layer and the Ni films. Information on the Fermi surface in such layered systems can improve our understanding of both the electrical transport and the origin of magnetic coupling between the layers.

Ni films were evaporated at room temperature from an electron-beam heated rod onto a clean Cu(001) surface. A slight re-annealing to 420 K after deposition helped to improve the film crystallinity while interdiffusion could be kept low. Fig. 13.7 shows the measured Fermi surface maps for a 2.4 ML

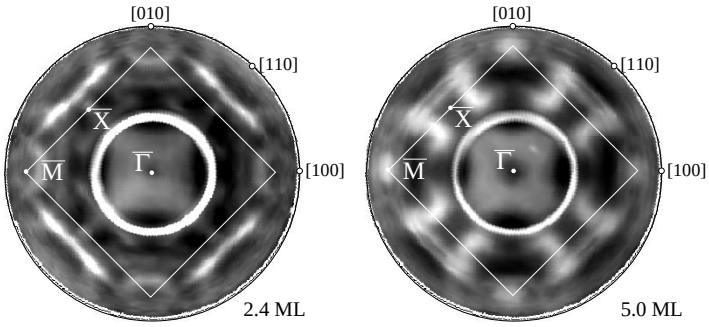

Figure 13.7: *Fermi surface maps of ultrathin films of Ni/Cu(001) measured by angle resolved photoelectron spectroscopy at a photon energy $h\nu$=21.22 eV. Both maps were taken at a sample temperature of T=150 K. The different contours observed at thicknesses of 2.4 ML and 5.0 ML are discussed in the text. The bright rings are an artefact of photons scattered into the analyzer. Figure from [3].*

thick and a 5.0 ML thick film. Both data sets were acquired at a sample temperature of T=150 K. The prominent ring feature in the center of these maps is an artifact caused by parasitic electrons that are excited when the light is directly reflected off the sample into the electron analyser. The thickness dependence of the Curie temperature leads to a paramagnetic state in the 2.4 ML thick film and a ferromagnetic state in the 5.0 ML thick film. The paramagnetic-to-ferromagnetic transition shows up in these data by the opening of an exchange splitting of the straight sp-band Fermi surface contours outside the $\overline{X}$-point as seen in the map for the 5.0 ML thick film. Otherwise, these features as well as the cushion shape in the centre of the plot are not changing much. More drastic changes are seen in the other contours, namely the d-band features around the $\overline{M}$-point, which change from a ring at 2.4 ML to a blot in the thicker film, or the line feature inside of the $\overline{X}$-point, which disappears at higher film thickness and is replaced by an entirely different structure. A comparison to band structure calculations reveals that the Fermi surface observed in the 5.0 ML thick film is indeed very similar to the one of bulk nickel, while a two-dimensional confinement is observed in the 2.4 ML thick film. This transition is, however, only observed for the electronic states derived from the Ni *d*-band, while the less localized *sp*-electrons exhibit a bulk-like Fermi surface at all film thicknesses.

[1] C. Pampuch, O.Rader, R. KlŁsges, C. Carbone, Phys.Rev.B **63** (2001) 153 409.

[2] G.J. Mankey, K. Subramanian, R.L. Stockbauer, R.L. Kurz, Phys.Rev.Lett.**78** (1997) 1146.

[3] M. Hoesch, PhD thesis, Univ. Zürich 2002.

13.7 Hexagonal boron nitride on Ni(111): defects and two-domain monolayers

A single monolayer of hexagonal boron nitride ($h-$BN) on Ni(111) forms an atomically sharp interface and can be used as a model substrate with low surface energy [1; 2; 3]. In this context line defects that we discovered in the nearly perfect $h-$BN monolayers play an important role. They influence e.g. the growth behaviour of metals on $h-$BN/Ni(111) [4]. Experiments combining scanning tunnelling microscopy (STM) and photoelectron diffraction (XPD) on the very same surface give an explanation for these defect lines in terms of a stacking fault. They appear on boundaries between different $h-$BN domains. Besides the original domain that dominates well prepared $h-$BN monolayers, the appearance of a second minority domain is triggered by impurities.
Fig. 13.8 illustrates these findings on the basis of two sub-monolayer preparations (P_1, P_2) yielding

$h-$BN islands on Ni(111). The XPD pattern in Fig. 13.8a) (P_1) reflects the well known original domain, with N atoms on top of the outermost Ni atoms and B atoms stacked on fcc sites (N,B)=(*top*,*fcc*) [2; 3]. The STM images in the conductivity mode (Fig. 13.8b) are dominated by triangular $h-$BN islands pointing in the $[\bar{1}\bar{1}2]$ direction. With respect to the B atoms the islands terminate with B-type steps (i.e. (111) nanofacets). In order to satisfy bond saturation we expect island rims with hydrogen saturated nitrogen chains. Fig. 13.8c) shows the resulting structural model. Preparation P_2 results in a diffraction pattern (Fig. 13.8d)) and in triangle directions (Fig. 13.8e)) rotated by 60° relative to the original ones. Fig. 13.8f) displays the model for this second domain with N atoms on top and B atoms on hcp sites (N,B)=(*top*,*hcp*). Here the boron atoms are hcp stacked and the islands terminate as well with B-type steps. Based on the structural models for the two domains (Fig. 13.8c) and f)) and the fact

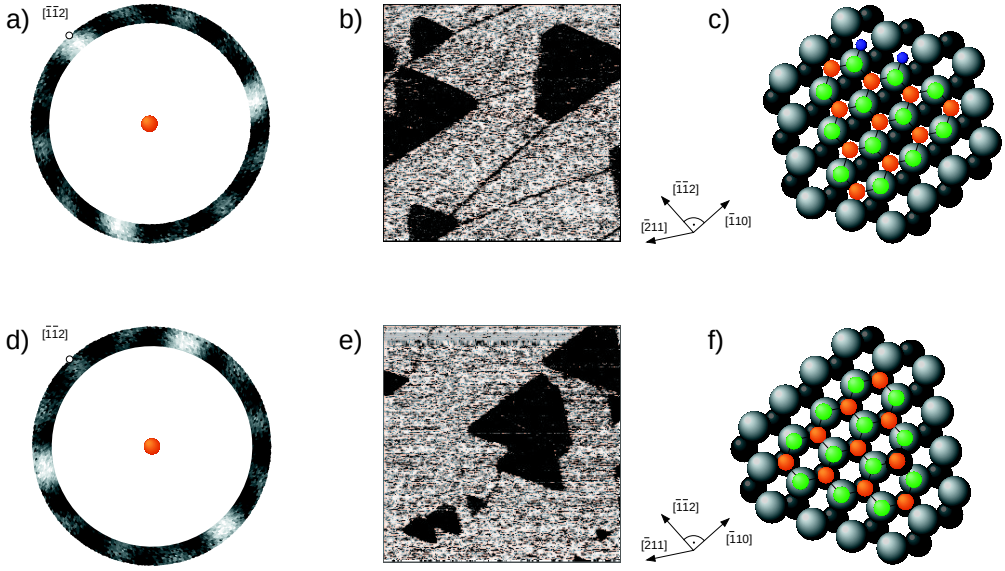

Figure 13.8: *XPD and STM results on $h-$BN islands partially covering the Ni substrate for preparation P_1 (a-c) and P_2 (d-e):*
a) Si $K\alpha$ excited B 1s XPD pattern. The three-fold maxima coincide with the $[\bar{1}\bar{1}2]$ directions.
b) a corresponding conductivity image (0.4μm×0.4μm, I=1 nA, V=-0.8 V). The $h-$BN triangles (black) point towards $[\bar{1}\bar{1}2]$ (the dark lines represent steps which induce a slight contrast).
*c) Top view of a model representing the island structure in b): the configuration is (N,B)=(*top,fcc*).*
d) Si $K\alpha$ excited B 1s XPD pattern. The main maxima point towards the $[\bar{2}11]$ direction.
e) a corresponding conductivity image (0.4μm×0.4μm, I=3 nA, V=-0.6 V). The $h-$BN triangles (black) are oriented towards $[\bar{2}11]$.
*f) Top view of a model representing the island structure in e): the configuration is (N,B)=(*top,hcp*).*

that line defects are found whenever two opposite triangles collide (not shown), an intuitive explanation for the defect lines is given: due to the different registry to the substrate, the two domains can not grow together and a linear imperfection (domain boundary) appears in between the fcc and the hcp domain. It is interesting to note that the second domain (i.e. (N,B)=(*top*,*hcp*)) which more likely appears on poorly prepared sample surfaces, was predicted by DFT calculations to be energetically only slightly less favourable (9 meV/BN unit) than the original (N,B)=(*top*,*fcc*) domain [5].

[1] A. Nagashima, N. Tejima, Y. Gamou, T. Kawai, and C. Oshima, Phys. Rev. B **51** (1995) 4606.
[2] W. Auwärter, T.J. Kreutz, T. Greber, J. Osterwalder , Surf. Sci. **429** (1999) 229 .

[3] M. Muntwiler, W. Auwärter, F. Baumberger, M. Hoesch, T. Greber, J. Osterwalder , Surf. Sci. **472** (2000) 125.

[4] W. Auwärter, M. Muntwiler, T. Greber, J. Osterwalder, Surf. Sci. **511** (2002) 379.

[5] G.B. Grad, P. Blaha, K. Schwarz, W. Auwärter, and T. Greber, submitted.

13.8 Adsorption and self-organization of C_{60} molecules on Cu(221)

Since the discovery of C_{60}, many studies have been performed in order to understand the basic properties of this complex molecule and to develop possible applications. An important issue concerns the fabrication of low-dimensional systems, where intriguing phenomena have been observed, such as Fermi gap opening in the C_{60} monolayer on Ag(100) [1] or superconductivity at alkali metal doped C_{60} surfaces at low temperature [2]. Depending on the substrate, single layers of C_{60} molecules have been found in different geometrical arrangements and different bonding and charge states. On Cu(111), C_{60} molecules form an ordered monolayer system, and photoelectron diffraction experiments showed that the molecules are adsorbed with a $6-$ring towards the surface, in two azimuthally equivalent orientations [3].

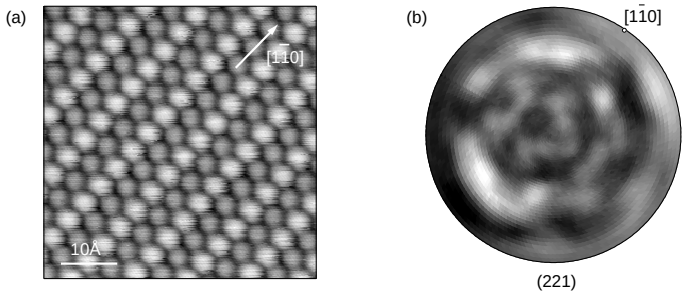

Figure 13.9: *One monolayer of C_{60} adsorbed on Cu(221). (a) Room temperature STM image showing alternating bright and dim rows of C_{60} molecules running along the step direction $[1\bar{1}0]$. (b) Experimental C1s XPD pattern (Mg Kα, $E_{kin} = 970eV$). The diffraction intensities are shown in stereographic projection and on a linear grey scale with maximum intensity corresponding to white.*

In order to orient these molecules and to align them into one-dimensional chains, we investigate C_{60} on vicinal surfaces. One monolayer of C_{60} on Cu(221) forms a quasi-hexagonal close$-$packed arrangement slightly relaxed in the direction perpendicular to the steps as we conclude from the LEED pattern. STM images show that C_{60} and Cu(221) self-organize into well ordered one-dimensional structures. The images indicate large terraces on which the molecules align themselves in parallel rows (Fig.13.9a)). On each terrace the rows have a regular modulation of the brightness. The unit cell contains two C_{60} molecules: a molecule that appears bright and a molecule that appears dim. This contrast can be explained in terms of different coordination to the substrate. From the XPD data in Fig.13.9(b) it can be concluded that at least in one of the two types of chains, the molecules have a single well-defined orientation.

[1] C. Cepek, I. Vobornik, A. Goldoni, E. Magnano, G. Selavggi, J. Kröger, G. Panaccione, G. Rossi, M. Sancrotti, Phys.Rev.Lett.**86** (2001) 3100.

[2] R. Hesper, L.H. Tjeng, A. Heeres, G.A. Sawatzky, Phys.Rev.Lett.**85** (2000) 1970.

[3] R. Fasel, P. Aebi, R.G. Agostino, D. Naumovic, J. Osterwalder, A. Santaniello, L. Schlapbach, Phys.Rev.Lett.**76** (1996) 4733.

13.9 Cysteine on Cu(110) studied with X-ray photoelectron diffraction

in collaboration with:
C. Quitmann, Swiss Light Source, Paul Scherrer Institut, 5232 Villigen, Switzerland

In the emerging field of nanotechnology, the adsorption of large molecules on surfaces plays a vital role in areas such as molecular electronics, nanodevices, and molecular recognition [1; 2]. A key piece of information that forms the starting point of any understanding of adsorbate-surface interactions is the local bonding geometry. For molecules larger than a few atoms the determination of the adsorption geometry is by no means a trivial task. Most of the traditional methods fail in the case of molecules with more than four atoms. Angle scanned X-ray photoelectron diffraction (XPD) has the potential for structural investigations of more complex systems, as was demonstrated e.g. in the case of heptahelicene adsorbed on copper surfaces [3]. With the advent of third-generation synchrotrons, a new class of XPD experiments have become possible. If the coverage of the adsorbate under investigation is in the submonolayer range, it is crucial to choose a suitable photon energy to have a high photoemission cross-section on the one hand and to optimize the signal to background ratio on the other hand.

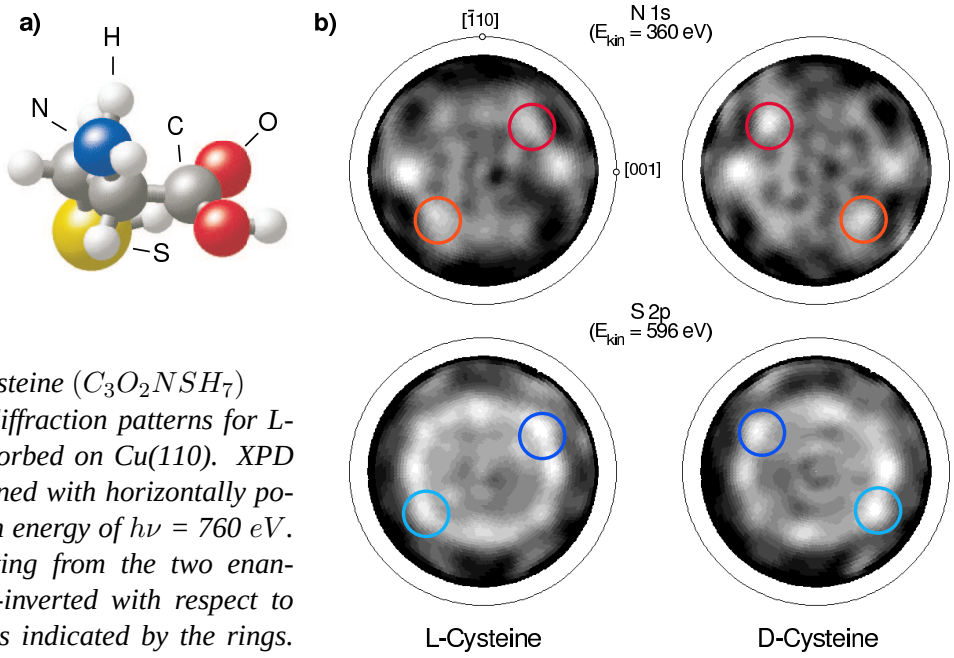

Figure 13.10: *a) Cysteine* $(C_3O_2NSH_7)$ *b) N 1s and S 2p diffraction patterns for L- and D-cysteine adsorbed on Cu(110). XPD patterns were obtained with horizontally polarized light with an energy of* $h\nu$ *= 760* eV*. The patterns resulting from the two enantiomers are mirror-inverted with respect to each other, which is indicated by the rings. The mirror plane is (001).*

During the last year we installed an endstation to perform angle resolved photoemission experiments at the Surface and Interface Microscopy (SIM) beamline at the SLS. In first experiments we deposited cysteine (Fig. 13.10(a)), a small amino-acid, onto a copper surface to study the adsorption geometry and the intramolecular rearrangement upon adsorption. We adsorbed a submonolayer of either D- or L-cysteine on a clean Cu(110) sample. In Fig. 13.10 the N 1s and S 2p XPD patterns are presented. All the patterns show clear forward scattering features (bright spots) with C_2 symmetry. They are mirror-inverted for opposite enantiomers. The chirality of the molecule is thus reflected in the patterns. The strongest forward scattering spots in the N 1s patterns correspond to scattering along the N-C axis. From the position of this spot the bonding angle of the N-C axis and the angle between this axis and the copper rows of the (110) surface can be directly determined. It is concluded that the molecules are adsorbed in two distinct azimuthal orientations. The structure will be retrieved by

comparing the experimental data to a set of scattering calculations in a trial and error approach.

[1] C. Joachim, J.K. Gimzewski, A. Aviram, Nature **408**, 541 (2000).

[2] F. Moresco et al., Phys. Rev. Lett. **86**, 672 (2001).

[3] R. Fasel, A. Cossy, K.-H. Ernst, F. Baumberger, T. Greber, J. Osterwalder, J. Chem. Phys. **115**, 1020 (2001).

13.10 Time-resolved electron diffraction

Real-time measurements of electron and atom dynamics on solid surfaces with picosecond time resolution are carried out in the so-called pump-probe mode: A strong first laser pulse puts the system under investigation into a specific state. In the simplest case the pump pulse is absorbed leading to a transient temperature rise in the surface. From this initial state the system evolves and is probed by a second time-delayed pulse (probe). The probe signal as function of delay time yields finally information about the evolution of the system.

Since several years we are to realize an experiment in which low-energy electrons are used as a time-resolved structure sensitive probe. The intensity of diffraction spots in patterns obtained from samples surfaces is then recorded as function of delay time. The experimental setup has been completed in April 2002 with the installation of a regenerative pulse amplifier (RegA) and an optic-parametric amplifier (OPA). The system purchased (Coherent Inc.) was chosen because of its high pulse repetition rate (250 kHz) and sufficient pulse energy (4 μJ). The OPA converts the high-intensity pulses of the RegA into tunable light pulses, the frequency of which covers almost the whole visible range from 450 nm to 750 nm. Meanwhile, the whole experiment was fully automated: delay stage and the CCD camera used to take the diffraction images are controlled by a host computer, and several analog voltages can be measured simultaneously. The program further allows autocorrelation experiments or voltage charts to be measured [1].

In order to acquire experience, the first pump-probe experiments were carried out using an electron gun designed for operation at medium and high energies (more than 1 keV)[2]. This gun has the advantage of producing a rather high electron current allowing optical filters, scattering geometry, detector settings, and other important parameters to be optimized. As start experiment, the transient temperature rise of the lattice after absorption of the pump pulse is to be recorded as a function of time. For this purpose, the LEED spot intensity is used as an ultra-fast thermometer (see e.g. Ref. [3]). A rise in temperature results in a decrease in spot intensity due to the Debye-Waller effect. The thermometer can be calibrated in a static experiment by measuring the spot intensity for various temperatures. Such a calibration curve is depicted in Fig. 13.11. In the inset, raw data are shown as example for a typical LEED pattern as obtained with the high-energy electron gun from Ge(111). Faint spots of the c(2x8) surface reconstruction are visible between the principal diffraction spots emphasizing the high quality of these images.

Despite the excellent signal-to-background ratio of these images, all attempts to record time-resolved data failed so far for several reasons : 1.) Spatial overlap to within a few micrometers is difficult to obtain and to maintain for electrons and photons on a distance of meters. This problem could partially be solved by attaching a channeltron detector with pinhole close to the sample position. 2.) Temporal overlap, *i.e.* the delay "zero" for which electrons and photons arrive at the same time on the sample, has to be determined in advance based on ray-tracing calculations. Since, in this gun, the electrons are slow and the path length of 0.5 m is very large, the uncertainty of these calculations is quite

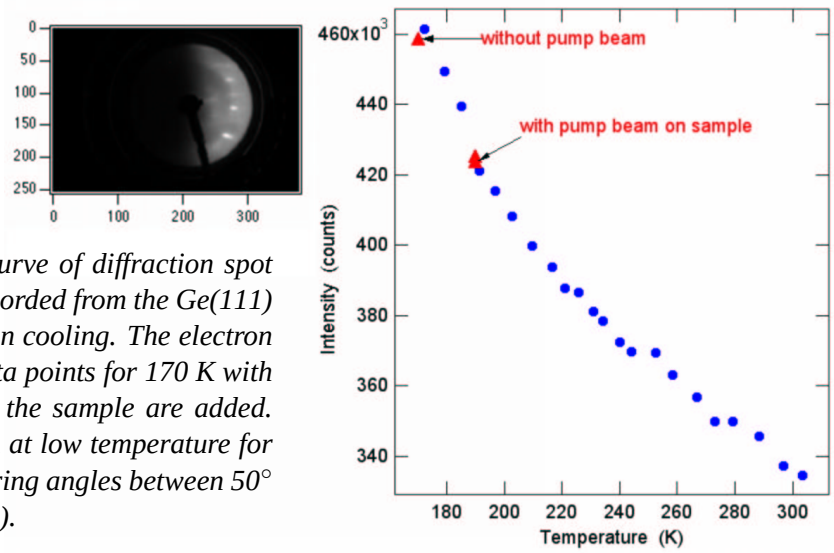

Figure 13.11: *Calibration curve of diffraction spot intensity vs. temperature, recorded from the Ge(111) surface during liquid nitrogen cooling. The electron energy was 200 eV; some data points for 170 K with and without pump beam on the sample are added. Inset : typical LEED pattern at low temperature for normal incidence and scattering angles between 50° and 90° (cut-off of the image).*

large. Again, by means of the channeltron detector this uncertainty could be reduced to smaller than 1 ns, which is within the range of the delay stage used here. 3.) Temporal broadening of the electron pulses, caused by the initial velocity distribution and path length differences. The velocity distribution is determined by the work function of the photocathode and the photon energy. The photon energy, which can be tuned by means of the OPA was set close to half the work function of the cathode , leading to 0.3 eV spread in energy for the two-photon-photoemission current. Nevertheless, due to the long flight time, this results in a temporal broadening of the order of 100 ps. Space charge may lead to similar broadening. However, this latter effect was found to become important for photocurrents higher than 100 pA at 250 kHz repetition rate, thus 2'000 photoelectrons per pulse. During pump-probe experiments, the photocurrent employed was held below 20 pA by reducing the probe light intensity. Some of the time dependent curves taken from Ge(111), pumped with 800 nm light and a fluence of about 10 mJ/cm^2, showed the expected signal but were not reproducible.

Finally, the OPA turned out to be often instable on the time scale of several hours, rendering the data analysis difficult. High harmonic generation (like the third harmonic at 266 nm, for instance) is much more stable than parametric amplification. In collaboration with P. Hamm and J. Helbing from the Physical Chemistry Institute, a setup for third harmonic generation from 800 nm light was mounted, based on frequency doubling in a type-I BBO crystal and subsequent sum frequency generation in a type-II BBO crystal. Due to the high photon energy, however, absorption in lens and window materials becomes important, and this project was postponed.

After these preliminary experiments, the actual gun designed for low-energy electrons [4; 5] was mounted. It is expected to provide electron pulses with a temporal spread of the order of 5 ps. However, the low current output of this gun (a few fA at 250 kHz repetition rate) necessitates operation of the two-stage microchannel plate LEED detector at highest amplification level and the subtraction of dark reference images taken under the same conditions but without electrons. Typical CCD exposure times are of the order of ten minutes per image. Nevertheless, the first measurements are already promising. One curve, recorded from Ag(111) using 800 nm pump light at a fluence of 20 mJ/cm^2, is shown in Fig. 13.12 beside a typical image after subtraction of the dark image. Unfortunately, it was impossible to take advantage of the resonant surface plasmon absorption at 400 nm for the pump pulse [6], because stray light of these high-energy photons (3.15 eV) was found to produce strong background in the LEED detector. The step, which is seen in Figs. 13.12(b) and (c) close to the expected time "zero" is likely due to purely instrumental intensity fluctuations and thus not the result of a real thermal effect in the sample surface. Nevertheless, we hope that we will be able to record

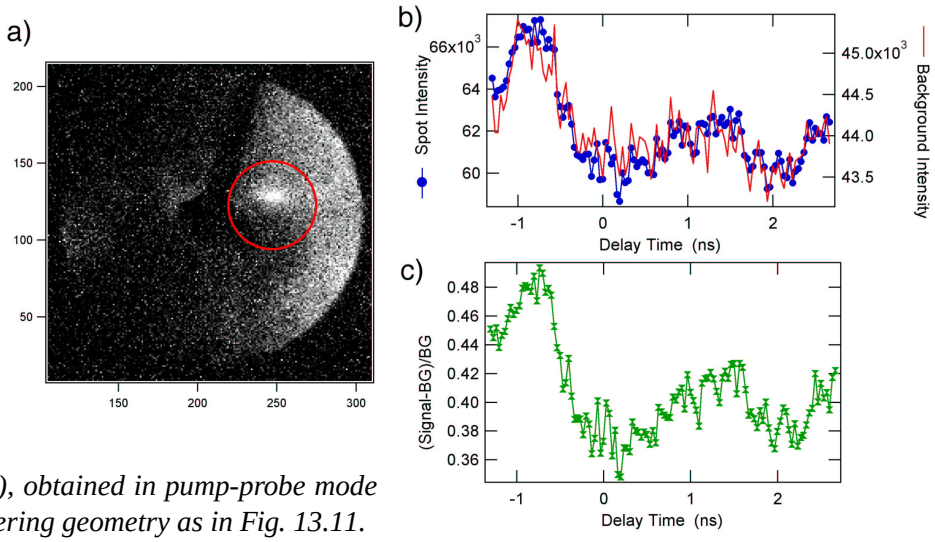

Figure 13.12:
Results from Ag(111), obtained in pump-probe mode using a similar scattering geometry as in Fig. 13.11.
a) One image from this series of 121 images after subtraction of a reference dark image; the LEED spot is highlightened by a red circle.
b) Spot (blue) and background (red) intensities
c) the normalized difference signal-background as function of delay time. The width of the step seen in all curves in (b) and (c) close to delay zero is about 200-250 ps. Since the background behaves in the same way, this step is probably due to fluctuations in the laser power and/or gun current.

time-resolved LEED images with picosecond resolution in near future.

[1] M. Barry, *Vorbereitende Arbeiten für zeitaufgelöste LEED-Experimente*, Diplomarbeit, Universität Zürich, 2002.

[2] M. Aeschlimann, E. Hull, C.A. Schuttenmaer, J. Cao, Y. Gao, D.A. Mantell, and H.E. Elsayed-Ali in *Time-resolved electron and x-ray diffraction*, P.M. Rentzepis (Ed.), Proc. SPIE **2521**, 103 (1995).

[3] X. Zeng, H.E. Elsayed-Ali, Phys. Rev. B **64**, 085410 (2001).

[4] R. Karrer, *Bau einer Elektronenkanone für zeitaufgelöste Beugung mit langsamen Elektronen*, Diplomarbeit, Universität Zürich, 2000.

[5] R. Karrer, H.J. Neff, M. Hengsberger, T. Greber, and J. Osterwalder, Rev. Sci. Instrum. **72**, 4404 (2001).

[6] J. Lehmann, M. Merschdorf, W. Pfeiffer, A. Thon, S. Voll, and G. Gerber, Phys.Rev.Lett.**85**, 2921 (2000).

13.11 Measurement of femtosecond pulses - autocorrelation

For any study of ultrafast processes by means of femtosecond laser systems, tools are needed for characterising the pulse shape, spectrum, and temporal width. Since the temporal width is of the order of a few tens of femtoseconds, too fast for any electronic device, reliable results about the width can only be obtained by correlation experiments. In this type of experiment, a pulse of comparable or even smaller width is used to measure the quantity of interest. If the two pulses originate from one single pulse by beam splitting, one speaks of autocorrelation. After the beamsplitter, both fractional pulses travel different path lengths such that one is delayed with respect to the other. At the end both

are brought back together in a non-linear process and the second-order signal is measured, like the second harmonic intensity obtained in a frequency-doubling crystal, for instance. The second-order yield depends on the product of the pulse intensities in contrast to a linear process, the output of which depends on the sum (see e.g. Ref. [1]). The second-order signal is therefore directly proportional to the autocorrelation function.

For this purpose, an autocorrelator was to be built which had the following specifications : low cost, smallest number of optical elements (for reasons of pulse broadening and alignment), and a fast scan rate such that it allows optical paths and pulse compression stages to be optimized for smallest temporal chirp. Further requirements would be the possible operation over a large range in wavelength (400-800 nm), and the possibility to measure the coherence time. The latter is given by Fourier transforming the frequency spectrum of the pulses and corresponds to the minimum pulse duration, which can be achieved for a given setup. The final autocorrelator design was based on a Michelson-Morley interferometer comprising one beamsplitter and two mirrors. This setup can easily be extended by using two further mirrors and a lens to a confocal arrangement for background suppression [1]. In one of the two branches, the mirror position and thereby the optical delay are moved by a piezocrystal, simply controlled by an analog voltage.

Initially, two-photon-photoemission from the photocathode of a photomultiplier tube (PMT) should be used as second-order signal. The PMT (Hamamatsu) is optimised for operation in the visible light range with a fairly sharp cut-off between 650 and 700 nm. Using this PMT, the setup was tested with 800 nm light. In the next step, the PMT should be replaced by a so-called solar-blind PMT having its cut-off wavelength in the ultraviolet. Thereby, a strong non-linear response is to be expected for the whole wavelength range of interest. The advantage of using a PMT are its fast response time and high quantum efficiency allowing for high scan rates on one hand and an amplified strong signal output on the other hand. Finally, it turned out that despite the sharp cut-off the linear response is still sufficiently strong at 800 nm to mask the second-order 2PPE signal.

The output, shown in Fig. 13.13 (a) and (b) represents therefore the interference pattern of the two pulses. The width of this pattern corresponds to the coherence length (and time) of the pulses, found to be 40 fs after deconvolution of the fitted Gaussian shape (full width at half maximum 56 fs). From an independent measurement of the pulse spectrum (Gaussian shape of 25 nm width at 795 nm central wavelength), 37 fs are obtained in good agreement with the value found here. The pulse duration at the output of the laser oscillator was measured to be 64 fs with a commercial autocorrelator.

It has to be noted that the ratio of linear to second-order response of the PMT depends critically on experimental parameters like light intensity and PMT voltage. However, no conclusive results have been obtained by optimising the output signal. Two-quanta photodiodes or solar-blind PMTs could be used in order to circumvent this problem. To this end, the true autocorrelation curve was measured, as shown in Fig. 13.13c, by introducing a frequency-doubling β-bariumborate (BBO) crystal in front of the detector and by removing the remnant fundamental light by appropriate filters. The curve was best fitted by assuming $(\mathrm{sech})^2$-pulse shape yielding 135 fs for the pulse duration after deconvolution. This value compares favourably to the value of 140 fs obtained with a commercial autocorrelator after an arrangement of filters and mirrors similar to the one used here.

[1] W. Demtröder, *Laser Spectroscopy, Basic Concepts and Instrumentation*, 2nd edition, pp 622-629, Springer (Berlin, Heidelberg, New York), 1998.

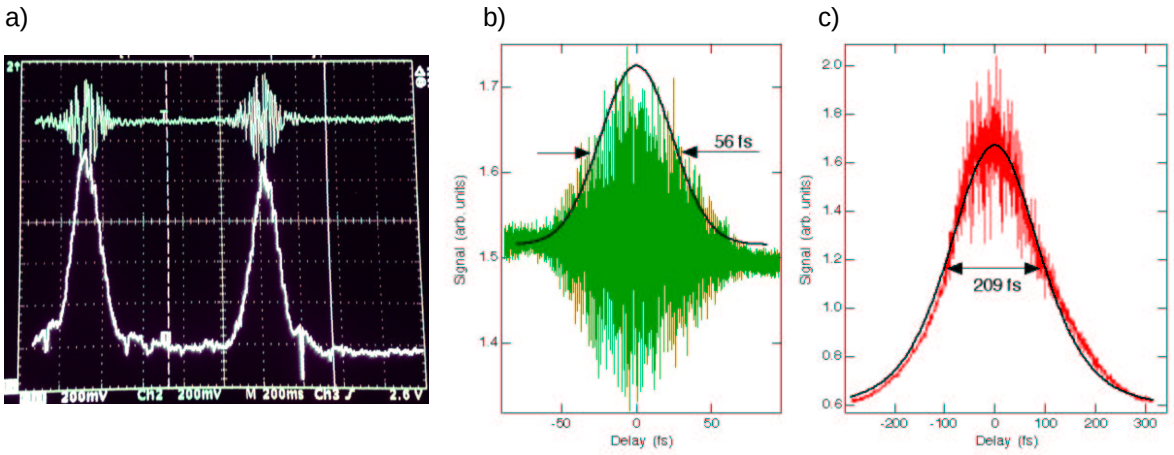

Figure 13.13: *Typical signals from the autocorrelator :*
a) Single shot measurements of the coherence length, recorded by means of an oscilloscope and a peak detector; the scanning rate was 0.33 Hz. The upper green curve are raw data from the PMT, the white curve underneath it is the envelope function as output from the peak detector.
b) Computer controlled measurement of the coherence length. The black line shows a Gaussian fitted to the envelope yielding the width of 56 fs.
c) Autocorrelation experiment recorded using a BBO crystal for frequency doubling. The autocorrelation width is found to be 209 fs. Note the obtained signal-to-background of 2:1 as theoretically expected for this setup.